



Unjamming strongly compressed rafts: Effects of the compression directionGregor Plohl , Mathieu Jannet, and Carole Planchette ^{*}*Institute of Fluid Mechanics and Heat Transfer, Graz University of Technology, Graz 8010, Austria*

(Received 25 March 2022; accepted 1 September 2022; published 16 September 2022)

We experimentally study the unjamming dynamics of strongly compressed particle rafts confined between two fixed walls and two movable barriers. The back barrier is made of an elastic band, whose deflection indicates the local stress. The front barrier is pierced by a gate, whose opening triggers local unjamming. Prior to gate opening, the rafts are quasistatically compressed by moving only one of the two barriers, in the vicinity of which folds form. Using high-speed imaging, we follow the raft relaxation with folded, jammed, and unjammed areas and measure the velocity fields inside and outside the confined domain. Two very different behaviors develop. For rafts compressed by the back barrier, only partial unjamming occurs. At the end of the process, many folds remain and the back stress does not relax. The flow develops mostly along the compression axis and the particles passing the gate form a dense raft whose width is the gate width. For rafts compressed at the front, quasitotal unjamming is observed. Almost no folds persist and only minimal stress remains, if any. The particles flow along the compression axis but also normally to it and form a rather circular and not dense assembly. Both the force chain network orientation and the initial fold location could cause the unjamming difference. Other effects, such as a different pressure field or simple steric hindrance, cannot be excluded.

DOI: [10.1103/PhysRevE.106.034903](https://doi.org/10.1103/PhysRevE.106.034903)**I. INTRODUCTION**

Capillary adsorbed particles at liquid interfaces have long been used in emulsions and foams [1–3]. Their potential for further applications, especially for producing bijels [4–6], chemical-free reversible encapsulation [7–10], and membranes [11], has renewed interest in them. In this context, one key attribute of the particles is their capacity to stabilize interfaces. This stabilization partly results from the large reduction of surface energy associated to particle adsorption. Further stabilization originates from the physical barrier the particles build that prevents direct contact with other surfaces. The effects resulting from these two stabilization mechanisms remain challenging to characterize at the macroscopic scale. The most common way consists of describing the interfacial mechanical properties. Thanks to intensive research, these properties are fairly well outlined for quasistatic regimes and moderate compression. Yet, for general conditions, they are poorly understood and therefore poorly predictable. This lack of knowledge is particularly profound for large strains and large strain rates or when strong gradients of particle coverage exists. For these conditions, commonly encountered in natural situations and industrial processes [12], barely no data exist. Consequently, key aspects such as self-healing capacity, self-healing dynamics, and, more generally, the processability of these interfaces remain widely unexplored. Our article aims to shed some light onto these topics.

Before detailing our method and findings, it is helpful to recall the existing knowledge about the mechanical properties of particle-laden interfaces. At moderate particle coverage, the interface is viscous. It becomes viscoelastic upon the particle network percolation, and finally behaves as a solid for greater

particle coverage [13–15]. The transition toward a solidlike behavior is associated to a pressure collapse [16,17] and attributed to a jamming process [18], a phenomenon common to other athermal assemblies, also called soft glassy materials [19,20]. If further compressed, the interface buckles, giving rise to regular wrinkles whose amplitude regularly increases, until one of them dramatically grows and eventually collapses into a large fold.

To date, most studies were motivated by practical interests, such as bubble dissolution arrest and foam stabilization [21–24]. Consequently, they have been focusing on the mechanical properties of interfaces prepared between the jamming and folding transitions. In this range, it has been shown that the interface can be modelled as a continuous media. This approach is based on the buckling of the interface subjected to quasistatic uniaxial compression. Similar buckling is observed for monolayers of irreversibly adsorbed molecules [25], membranes [26], and solid sheets [27,28]. The energy minimization selects a wavelength which results from the competition between bending and gravitational ironing. The selected wavelength gives the elastic Young modulus (for 3D approach) or the elastic bending modulus (for 2D approach) of the particle-laden interface [29]. This elastic modeling has proved to be valid for dynamic regimes too [30] but has failed when mixtures of small and large particles were used. In this case, deviations from the expected modulus were observed, which were attributed to possible variations of the stress transmission efficiency, potentially caused by the coexistence of different types of particle-particle contacts [31]. This observation with others, such as finite size effects in uniaxial compression [32], mechanical response under compression [22,33], raft fractures [34], inhomogeneous stress propagation [35,36], plasticity [9], etc. has evidenced the limit of the elastic model and points toward the granular character of these interfaces. Indeed, these limits are probably related to

^{*}carole.planchette@tugraz.at

the framework successfully developed for 2D granular media. In dry granular matter, *force chains* emerge which have been experimentally observed and numerically computed [37–40]. These force chains are suspected to build up in particle rafts too, where they could significantly modify the dynamical response [31,41]. Yet, dedicated investigations remain scarce and the present article constitutes a fundamental step in this direction.

More precisely, this article aims to understand how the above-mentioned granular character of the interface, evidenced for moderate strains and mostly under a quasistatic regime, affects its mechanical properties when subjected to large strains or fast strain rates. Said differently, is the granular character of the interface relevant for the relaxation of strongly compressed rafts? And what could be its effects? While answering these questions undoubtedly leads to a gain of fundamental knowledge, it also addresses a crucial practical aspect, known under the term of self-healing. In contrast to commonly used surfactants, the particles are irreversibly absorbed to the interface and can therefore not constitute reservoirs in the bulk, from where to migrate to feed freshly created interface areas [4,42]. While this aspect is positive to arrest bubble dissolution, it remains challenging for expending interfaces. A good strategy to efficiently overcome this challenge might be to establish particle reservoirs outside the bulk and, more particularly, in interfacial folds. In this context, the questions can be reformulated as such: Can particles located within folds become available to stabilize uncovered areas, providing self-healing capacity to these interfaces? Is this capacity, i.e., the portion of stored particles that can be efficiently released, influenced by the granular character of the interface? What about the kinetic of this supply, i.e., the self-healing dynamic?

We answer these questions by studying the dynamical relaxation of strongly compressed particle-laden interfaces and show that two typical behaviors are obtained, which appear to be mostly selected by the direction of compression. First, we describe the experimental methods. The results—obtained for two square rafts of same compression performed either from the back or front side—are then detailed. We show that similar extreme behaviors are obtained for less compressed rafts. We attribute this difference to a mechanical and directional effect, which causes (or not) relaxation arrest. The possible origins of what we call granular diodes are discussed in light of results obtained from rafts compressed on both sides. It may derive from the orientation of the chain force network, which either favors unjamming via the removal of keystone particles or prevents it by redirecting the stress toward the sides. It may also be related to the initial location of the folds, whose progressive reorientation either facilitates further relaxation or geometrically locks it. The article ends with the conclusions, which underline the consequences of our findings in terms of interface processability, self-healing capacity, and dynamics.

II. EXPERIMENTAL METHODS

A. Setup

As sketched in Fig. 1, the experimental setup consists of a rectangular trough with two fixed parallel walls separated

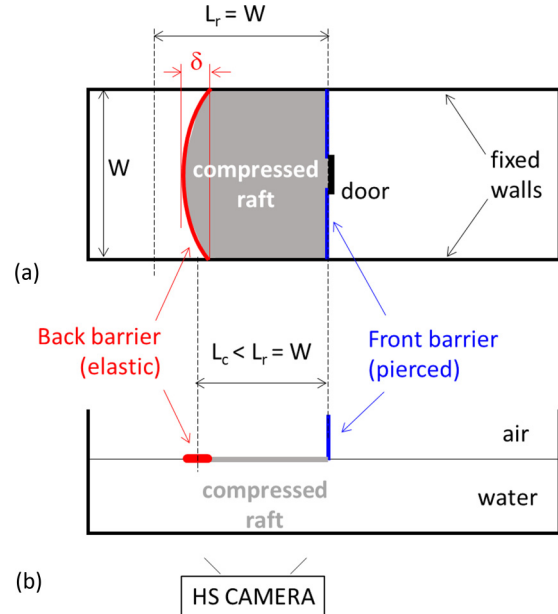


FIG. 1. Experimental setup sketched from (a) top and (b) side views. The particle raft relaxed length, L_r , is equal to its width, W . The raft is compressed by moving either the back barrier (red) or the front one (blue) to obtain a length $L_c < L_r$. The elastic deflection δ (exaggerated here) enables to calculate the local stress.

by 6 cm and two movable barriers that can be quasistatically translated along the two walls to compress the confined particle raft. Deionized water with a depth of 2 cm is used for all experiments. The so-called back barrier is made of an elastic string placed in the plane of the interface, perpendicularly to the side walls. As described in Appendix A, the string is produced in house by injecting a (1:1) mixture of Elite Double 8 basis and catalyst (Zhermack Spa) into a glass capillary, which is manually removed after the elastomer reticulation has been completed. The elastic is then fixed to a 6 cm broad structure and calibrated using known weights to obtain its Young modulus; see Appendix B. During the experiments, the elastic deflection, δ , is measured and used to calculate the stress developing at the back side of the raft. Details are given in Appendix C. The second barrier, referred to as a front barrier, is pierced in its center by an orifice of width $w = 1$ cm. A vertically sliding gate made of a thin plate enables us to maintain the orifice closed. By suddenly lifting the gate, the orifice gets instantaneously unblocked (in about 20–30 ms) and the applied stress is locally released.

B. Particles

The particles are sieved and silanized glass beads, whose density is $\rho_s = 2500 \text{ kg m}^{-3}$. The diameter distribution measured over pictures of more than 1000 particles corresponds to a Gaussian with a mean corresponding to $d = 107 \mu\text{m}$ and a standard deviation of 8.4%. After having cleaned the particles with a piranha solution, silanization is performed using solution of trichloro-perfluorooctylsilane in anhydrous hexane. All chemicals were purchased from Sigma-Aldrich and used as received. The resulting contact

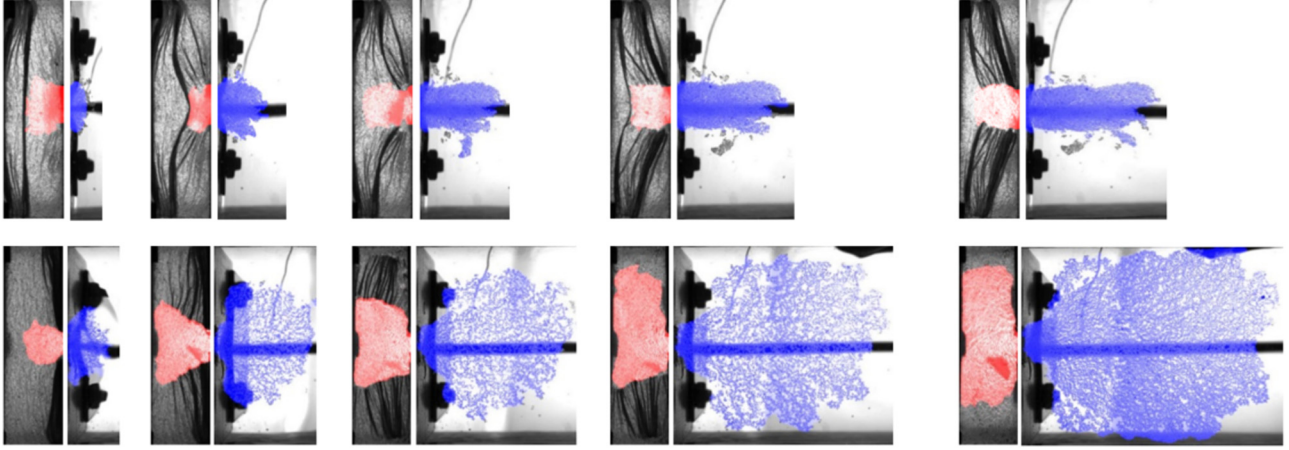


FIG. 2. Image sequences of strongly compressed rafts ($K = 67\%$) after local release of the stress achieved by lifting the gate of the front barrier. The opening instant is taken as time origin. The red color indicates unjammed particles area while the blue shows the escaped particles. Top: Back compression (subscript b) from left to right: $t_{b,1} = 70$ ms, $t_{b,2} = 120$ ms, $t_{b,3} = 250$ ms, $t_{b,4} = 360$ ms, and $t_{b,5} = 430$ ms. Bottom: Front compression (subscript f) from left to right: $t_{f,1} = 80$ ms, $t_{f,2} = 410$ ms, $t_{f,3} = 630$ ms, $t_{f,4} = 1600$ ms, and $t_{f,5} = 2800$ ms.

angle measured on single particles placed at the apex of a pendant drop is found to be $107^\circ \pm 10^\circ$.

C. Experimental procedure

The first step of the experimental procedure consists of obtaining square rafts. To do so, the trough is filled with distilled water and particles are sprinkled on the interface between the barriers. By blowing on them and gently pushing them with a pipette tip, we ensure that they distribute in a monolayer. This monolayer is then compressed and decompressed by moving any of the two barriers and the quantity of particles is adjusted to have a square relaxed raft. We define the raft as relaxed as soon as the stress measured during decompression vanishes. Noting L_r the relaxed length and W the trough width, we have $L_r = W = 6$ cm. Once a square raft is formed, the distance between the barriers is increased and the raft is annealed by stirring the particle assembly. The raft is then compressed again, but by moving only one of the two barriers, the other one remaining fixed. The state of compression is then given by $K = (L_r - L_c)/L_r$ with L_c the distance between the two barriers in their final position. Finally, the relaxation is triggered by suddenly opening the gate. Note that this last step, which marks the effective start of the experiment, is done after the raft has been compressed to the desired level, while the two barriers are immobile. A high-speed camera placed under the raft records the relaxation with 3000 frames per second and a resolution of $14.1 \mu\text{m}/\text{pixel}$. The movies are then analyzed to provide different quantities.

III. MEASUREMENTS

A. Unjammed, jammed, folded, and escaped areas

During the raft relaxation, several quantities are measured, which first need to be defined. The illustrative image sequences displayed in Fig. 2 are useful to do so. Let us first consider what happens in the initially confined domain. After the gate opens, some particles locally unjam. Here unjammed particles correspond to particles that move relative to each

other within the interface. Unjammed domains appear unbuckled. The associated surface area, denoted A_{uj}^* , is tracked using IMAGEJ with the machine learning plug-in called Trainable Weka Segmentation [43]. For better visualization, it is colored in red in Fig. 2. After normalization by the initial confined domain area $A_c = WL_c$, we obtain $A_{uj} = A_{uj}^*/A_c$. Per definition, the particles that remain jammed occupy the normalized area $A_j = 1 - A_{uj}$. Practically, these are particles that do not experience any individual motion. The corresponding surface appears buckled and potential movements, if any, are collective, limited to macroscopic folding or defolding, similarly to what an incompressible bidimensional solid membrane would do. We additionally measure the so-called folded surface area A_f^* . Practically, the folds correspond to interface portions which make a significant angle to the horizontal plane and therefore appear dark on the back-lighted pictures. Thus, A_f^* is obtained by using a threshold function and is then normalized by A_c to provide A_f . Note that this term refers to the projection of the folded surface and not to the surface area contained in these folds, which is not accessible with our images.

Let us now look at what happens outside of the initially confined domain. Some of the unjammed particles flow through the orifice and migrate further to form a more or less dense assembly, colored in blue in Fig. 2. The surface area occupied by this assembly, A_e^* , is tracked using a threshold function applied after subtraction of the background taken in the absence of particles. The normalized escaped area A_e is obtained by dividing A_e^* with $(L_r - L_c)W = A_r - A_c$, i.e., with the difference between the relaxed raft area and the one of the confined domain. This difference represents the surface that excessive particles would occupy if forming a dense relaxed raft.

B. Back stress

Additionally, the deflection of the elastic barrier, δ , is recorded and used to compute Π , the lineic pressure (or stress) developing at the back of the raft. See Appendixes A and B for rubber preparation and calibration details, respectively.

For details about the conversion of δ into Π , please read Appendix C.

C. Velocity fields

Finally, we use the PIVlab routine of MATLAB [44,45] to gain information about the velocity fields developing in these systems. In practice, we perform three types of particle image velocimetry (PIV).

The first one focuses on the flow inside the confined area, and more precisely within the unjammed area. To avoid wrong interpolations with movements taking place in the jammed raft, such as fold translation, masks corresponding to the identified unjammed areas (red regions in Fig. 2) are applied, limiting the analysis to the region of interest. The second analysis is similar and consists of performing PIV outside the confined domain using masks that correspond to the escaped assembly (blue regions in Fig. 2). Note that we further reduce the masks of about 5 mm on the orifice side, since the nonuniform background of this zone causes errors in the PIV.

These PIVs, typically performed with a time resolution of 300 Hz, provide the instantaneous velocity field inside and outside the confined domain. Due to the large number of frames, the results are difficult to visualize and interpret. To facilitate their analysis, we divide each relaxation into four subphases and compute for each of them the distribution of the velocity components parallel and normal to the compression axis (v_{\parallel} and v_{\perp}). The subphases correspond to the time lapse between two consecutive images of Fig. 2, i.e., to $t_{b,i} \leq T_{b,i} \leq t_{b,i+1}$ and $t_{f,i} \leq T_{f,i} \leq t_{f,i+1}$, with $1 \leq i \leq 4$, for the back and front compressions, respectively.

The third analysis deals with the velocity profile at the orifice. There we limit the analysis to a small zone covering the orifice and increase the time resolution to at least 600 Hz. The width of the analyzed area is the orifice width and its length is fixed to 10 mm. For each picture, the obtained velocity field is projected along the compression axis to provide the velocity profile $u(x)$, with $-w/2 \leq x \leq w/2$. The flow-rate equivalent mean velocity \bar{u} is then calculated as $\bar{u} = \frac{1}{w} \int_{-w/2}^{w/2} u(x) dx$.

IV. RESULTS AND DISCUSSION

Here and in the rest of this article, results obtained with front compression are presented as solid lines and full symbols while those corresponding to back compression are represented by dashed lines and empty symbols. The red color systematically indicates quantities related to the confined domain while blue is used for quantities defined outside.

A. Detailed analysis of rafts compressed at 67%

In this section, we present the results obtained for two rafts compressed at 67% by moving solely the front barrier or solely the back barrier. The corresponding movies are visible in Refs. [46,47] and illustrative image sequences are reproduced in Fig. 2. The unjammed area found in the confined domain, A_{uj}^* , is systematically colored in red and the surface occupied by the escaped particle assembly, A_e^* , in blue. These colored masks, automatically obtained by the image treatment (Sec. III A), are in very good agreement with the areas detected by the eyes and can therefore be

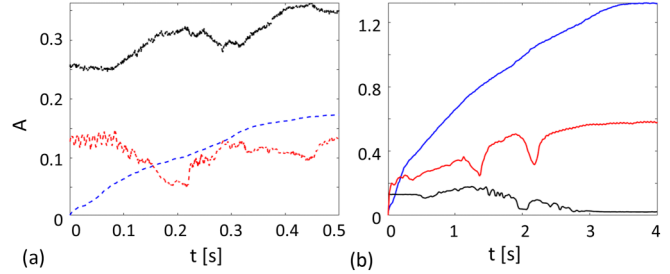


FIG. 3. Temporal evolution of A_{uj} (red), A_f (black) and A_e (blue) for (a) back- and (b) front-compressed rafts.

used for further analysis. The two rafts behave differently. For the back compression (top sequence), only a small zone found immediately behind the orifice unjams. The unjammed particles flow through the orifice, along the compression axis, to form a dense assembly whose width is the orifice width. The relaxation process stops while many folds are still visible. In contrast, the relaxation of the front compressed raft (bottom sequence) leads to important unjamming, which extends to almost all the rafts. The escaped particles form a large assembly of reduced density and broad width. No folds remain indicating a full relaxation. The relaxation of the back compressed raft is much shorter, almost stopping after 0.5 s, long before the one of the front compressed raft finishes, after 3 s.

To go further, we plot the temporal evolution of the normalized unjammed area A_{uj} (red), folded area A_f (black), and escaped assembly area A_e (blue). The curves, shown in Fig. 3, confirm the qualitative findings.

For the raft compressed from the back, slightly less than 15% of the initially confined area unjams and about 35% of the confined area appears folded at the end. Interestingly, the unjammed area does not significantly grow but rather fluctuates around its mean value. These fluctuations originate the folds dynamics. The folds, initially found at the back (Fig. 2, $t_{b,1} = 70$ ms) successively migrate toward the orifice. Each fold then transiently reduces the unjammed area ($t_{b,2} = 120$ ms) before disintegrating ($t_{b,3} = 250$ ms), explaining likewise the correlation between the local minimums of A_{uj} , at ≈ 0.2 s and ≈ 0.45 s, and the local maximums of A_f . The process is well visible in the movie of the Supplemental Material, see Ref. [46]. Finally, the particles that escape covers between 15% and 20% of the surface excessive particles would cover if forming a dense relaxed raft. This means that the large majority of the particles stored in the folds (at least 80%) cannot be made available to supply the surface initially free of particles. From a practical point of view, the self-healing capacity of such interfaces appear very limited under the present conditions.

Let us now consider the raft compressed to the same level but from the front side. The evolution of the unjammed, folded, and escaped areas appear to be totally different, see Fig. 3(b). About 60% of the initially confined area unjams. The folded area, which represents at maximum 15% of the confined area totally vanishes. Here as well, the evolution of these two quantities seem to be correlated as indicated by the coincidence of the local minimums of A_{uj} with the local maximums of A_f , found around 1.4s and 2.2s. Yet, in contrast

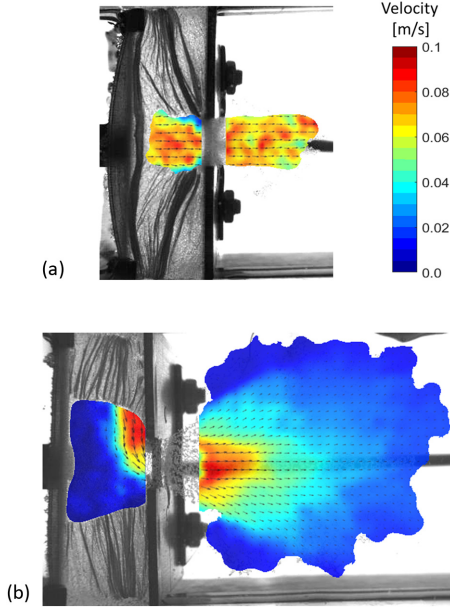


FIG. 4. Exemplary results of the PIV for (a) back compressed raft, $t_b = 0.28$ s, and (b) front compressed raft, $t_f = 1.28$ s.

to back compressed raft, these events do not correspond to the migration, expansion, and disintegration of individual folds but to the elimination of two larger folded blocks, found on both sides of the orifice, see movie in Ref. [47]. The first elimination takes place between the third ($t_{f,3} = 0.63$ s) and fourth ($t_{f,4} = 1.6$ s) pictures of Fig. 2 while the second one occurs between the fourth ($t_{f,4} = 1.6$ s) and fifth ($t_{f,5} = 2.8$ s) pictures. Beside these two bumps, A_{uj} continuously increases while A_f decreases. Almost all particles initially stored in folds unjam and migrate through the orifice to cover a surface that is 1.3 times the excessive surface given by $A_r - A_e$. While a value larger than 1 can first be surprising, it is well explained by the fact that the assembly of escaped particles is less dense than the relaxed raft. The relaxed raft coverage or density is close to the one of jamming, defined as $\varphi_j = \pi/2\sqrt{3} \approx 0.91$. The one of the escaped assembly can be only roughly estimated from our pictures, providing $\varphi_e \approx 0.74$, in agreement with 0.76, the value required to obtain particle surface conservation under total unjamming and given by $\varphi_e = \varphi_j/A_e$. These results clearly show that if the compression direction is favorable, the self-healing capacity of particle-laden interfaces can become important and approach its theoretical maximum. This maximum is found when all particles initially stored into folds are effectively released to cover initially free interface.

At this stage, it is difficult to draw conclusions about the self-healing dynamics. For the front compressed raft, only 0.12 s are required to obtain $A_e = 15\%$ by comparison to 0.33 s for the back compressed raft. Yet, this rate quickly slows down. If calculated over a longer time period (2 s), it is found to be $\dot{A}_e = 0.5 \text{ s}^{-1}$, comparable to 0.45 s^{-1} , the rather constant rate obtained for back compression.

To better understand the relaxation dynamics, we perform PIV on the unjammed areas found inside and outside the initially confined domain. Representative snapshots of the results are shown in Fig. 4. For the back compressed raft,

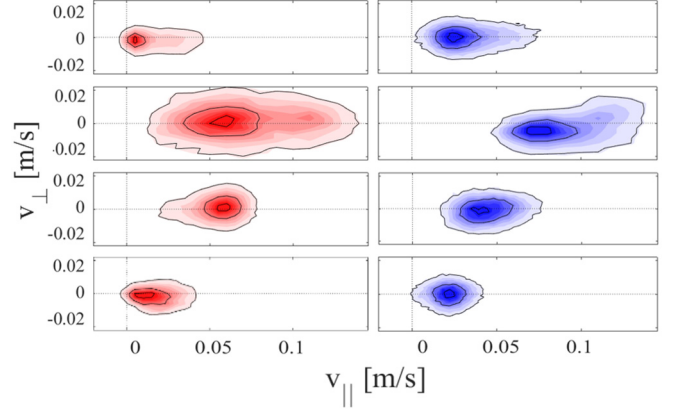


FIG. 5. Normalized velocity distribution for back compressed raft. Left (red): Unjammed area inside the confined domain; right (blue): escaped particles outside of it. From top to bottom, subphases $T_{b,1}$, $T_{b,2}$, $T_{b,3}$, $T_{b,4}$. The contours correspond to 0.1, 0.5 and 0.9 of the maximum value.

both the velocity magnitude and direction are uniform. The vectors clearly indicate a flow in the compression direction, from the back of the raft to the orifice and beyond. In contrast, the front compression gives rise to local acceleration, especially close to the orifice. Furthermore, velocity components perpendicular to the compression direction develop. Interestingly, the velocity field of the unjammed particles inside the confined domain is not symmetric. This can be explained by the selected instant, 1.28 s, which marks the beginning of the elimination of the first folded block, located on the upper part of the pictures (see Fig. 2) or movie (available from Ref. [47]). The second block, located on the opposite side of the orifice follows later, as already indicated, shortly after 2.0 s.

The PIV results obtained over the whole process are thus used to compute the velocity distribution on the subphases defined in Sec. III C. They are shown in Figs. 5 and 6 for back and front compressed rafts, respectively. For the back compressed raft, the velocity fields inside (red) and outside (blue) of the confined domain are always very similar, confirming that the unjammed particles form a cohesive assembly, which moves as a block. The velocity component perpendicular to the compression axis, v_{\perp} , is centered in zero and shows very small fluctuations, the 50% contour being comprised in ± 0.01 m/s. This is not the case of the parallel component, v_{\parallel} , which has positive values along the whole process. The flow from the back to the front shows some variations with a maximum during $T_{b,2}$, i.e., when the first fold disintegrates. Its mean value (0.07 m/s) and the fluctuations around it (-0.03 m/s and 0.07 m/s) then decrease until the end of the process. The velocity fields that develop for the front compressed raft are different. The correspondence between inside and outside is lost, which may indicate a certain independence of the two flows. Inside the confined domain (red), significant motion develops perpendicular to the compression axis leading to v_{\perp} values as large as v_{\parallel} values. The flow is not symmetric across the compression axis; see, for example, $T_{f,3}$ or $T_{f,4}$ for which $-0.01 \text{ m/s} \lesssim v_{\perp} \lesssim +0.11 \text{ m/s}$ and $-0.06 \text{ m/s} \lesssim v_{\parallel} \lesssim 0.01 \text{ m/s}$, respectively. This profound asymmetry corresponds to the successive

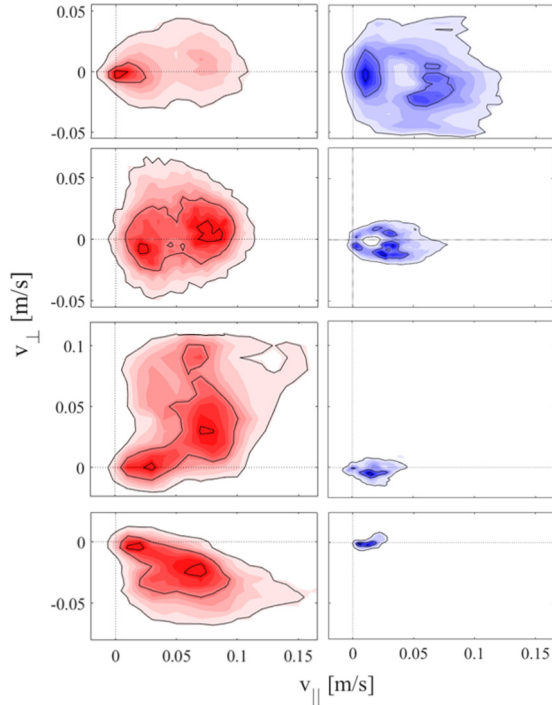


FIG. 6. Normalized velocity distribution for front compressed raft. Left (red): Unjammed area inside the confined domain; right (blue): escaped particles outside of it. From top to bottom, subphases $T_{f,1}$, $T_{f,2}$, $T_{f,3}$, $T_{f,4}$. The contours correspond to 0.1, 0.5 and 0.9 of the maximum value.

dislocation of two large folded blocks found on each side of the orifice. While passing through the orifice, the particles recover a symmetric velocity field (see blue maps). One can suppose that the shear they experience at this point overcomes the capillary attraction, forcing them to rearrange and explaining the reduced density. Finally, the focus of the velocities toward zero can rather be attributed to a normalizing effect than to changes in the flow. The increasing investigated surface area (A_e) contains an increasing number of points with low velocity, typically located at the assembly periphery, and therefore focuses the normalized distribution.

Despite the important disparities between the front and back compressed rafts, the velocity profiles at the orifice first seem rather similar, as shown in Fig. 7. The shape of the profile, the maximum value, approximately 0.15 m/s, and the fluctuation magnitude, in the order of ± 0.05 m/s, are comparable. The typical values, 0.10 m/s, are similar and cannot be immediately understood by considering the emptying of a bidimensional reservoir subjected to a pressure Π of 50 mN/m, the typical value given by the elastic

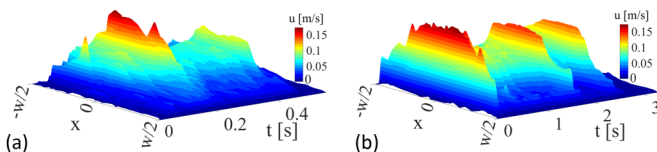


FIG. 7. Velocity profiles at the gate, $u(x)$, as a function of time, t , for (a) back and (b) front compressions.

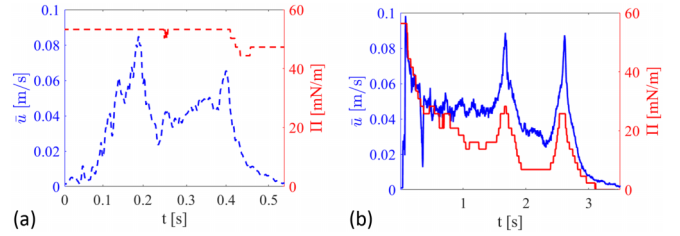


FIG. 8. Temporal evolution of \bar{u} (blue) and Π (red) for (a) back compression and (b) front compression.

deflection. Assuming the liquid is inviscid and adapting the classical Bernoulli equation, we estimate the velocity as $v_i = \sqrt{2\Pi/\rho_{\text{raft}}}$, where the bidimensional raft density is $\rho_{\text{raft}} = \varphi_j \rho_s 2d/3$. This provides $v_i \approx 0.79$ m/s, well above the measured value. Accounting for viscous losses is not straightforward since the raft viscosity is unknown. Instead, frictional losses may be considered. Yet, the raft relaxation neither corresponds to a constant acceleration (Beverloo law) nor to a constant velocity (forced discharge [48]), which prevents direct comparisons [49].

The particle flux and its fluctuations are then analyzed using the mean velocity \bar{u} . The results are plotted in Fig. 8 together with Π , the stress measured at the back.

Two points are worth being discussed. First, the different evolution of \bar{u} for the front- and back-compressed rafts. For the back compression, after a short transient phase and before the relaxation stops, \bar{u} seems rather constant. The two peaks, attributed to the disintegration of two successive folds (see Figs. 2 and 3), can be identified but no clear increase or decrease of \bar{u} over time can be seen. It is not the case of the front compressed raft for which \bar{u} clearly decreases over time. Fluctuations are perturbing this evolution but they can be well explained by the already mentioned elimination of the two folded blocks found on each side of the orifice. This confirms that the compression direction does not only influence the self-healing capacity but also its kinetics. The second important point, evidenced by Fig. 8, concerns the stress measured at the back of the raft. The latter remains almost unchanged for the back compressed raft, indicating that an important fraction of the initially applied stress remains. This remaining stress most likely originates the still-compressed domains found on each side of the central unjammed corridor. A closer look at the curve indicates a slight and possibly stepwise decrease of Π after each fold disintegration. If confirmed, such variations are typical of a solidlike behavior, for which the stress and strain are linearly connected via the Young modulus. For the front compressed raft, the stress totally relaxes. Interestingly, fluctuations are observed that correspond to the ones of \bar{u} , indicating a direct and almost instantaneous transmission of the stress through the entire raft. This could be interpreted as a liquidlike behavior, for which the stress and strain rate are proportional—the proportionality coefficient being the viscosity.

B. Generalization and phenomenological interpretation

The above-presented results were obtained on two similar rafts and generalizing these findings requires more data. Thus,

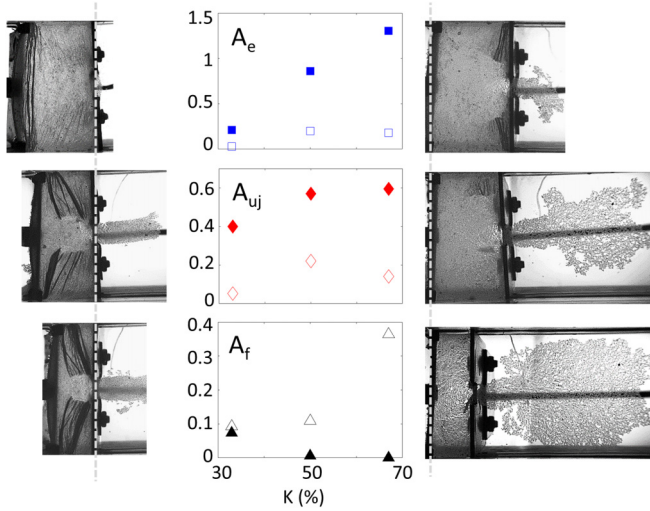


FIG. 9. Plots (central row): Final values of A_e , A_{uj} , and A_f as a function of K with empty (full) symbols for back (front) compression. Pictures: Final relaxation states obtained for back (left row) and front (right row) compressed rafts. From top to bottom, the raft compression is : $K = 33\%$, 50% , and 67% .

these experiments were repeated with two other pairs of rafts, compressed either from the front or from the back, with a compression level of 33% and 50% , respectively.

The final relaxation states, characterized in Fig. 9, appear to be mostly fixed by the compression direction. For rafts compressed on the back, the relaxation is partial, folds remain, and the escaped particles form a rather dense assembly, whose width is the orifice width. Similar rafts compressed from the front give rise to a quite different outcome. The relaxation is almost total, only a few folds remain, if any, and the escaped particles form less dense assemblies, whose width is much greater than the orifice width. A more quantitative description is shown in the central plots where A_e (squares), A_{uj} (diamonds), and A_f (triangles) are reported as a function of K . Whatever the level of compression, the relaxation of the front compressed rafts (full symbols) is always much more developed than the one of the back compressed rafts (empty symbols): A_e and A_{uj} are 4 to 8 times and 3 to 8 times larger, respectively, and A_f remains below 0.1 instead of ranging from 0.1 to 0.4. For back-compressed rafts, K has limited influence on A_e and A_{uj} but strong effects on A_f . For front compression, the influence of K on A_e and A_{uj} is significant. The greater the compression, the greater these two quantities. The effect is stronger for A_e than for A_{uj} , which could be explained by variations of the assembly density. Indeed, the surface occupied by a given number of escaped particles is modulated by the packing of the assembly, which may decrease with increasing compression (or flow velocity). Folds are very limited, which is expected given the large scale of unjamming.

From a practical point of view, these results indicate that, for the studied geometry, the self-healing capacity of particle-laden interfaces is principally a function of the compression direction. For a given direction, the greater the compression, the greater the fraction of stored particles can flow and cover initially particle free regions. This released fraction is always much larger for front than for back compression.

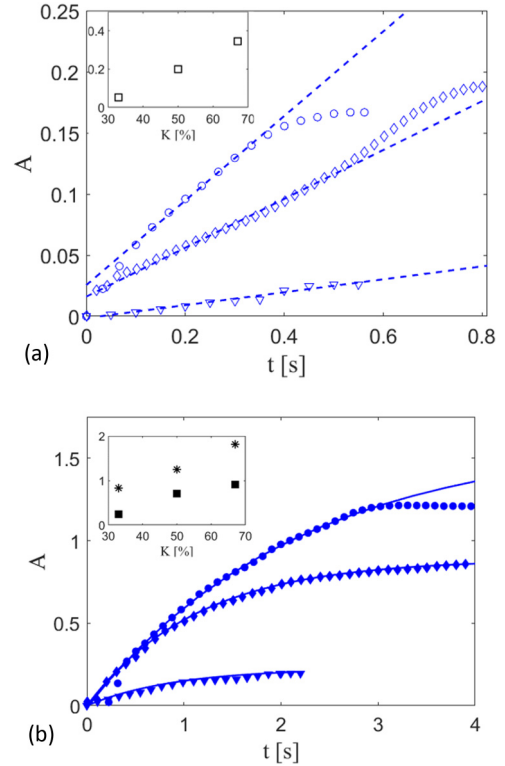


FIG. 10. $A_e(t)$ for (a) back and (b) front compressed rafts. Symbols are experimental data with triangles for $K = 33\%$, diamonds for $K = 50\%$, and circles for $K = 67\%$. The dashed and continuous lines are linear and exponential fits given by Eq. (3) and (4), respectively. Insets: $\dot{A}_e(t = 0)$ (squares) and τ (stars, if applicable) as a function of K .

To go further and better assess the potential of folds to be used as particle reservoirs, the dynamics of this release should be characterized. We therefore plot in Fig. 10 the temporal evolution of A_e for all studied rafts. The back compression does not only limit the magnitude of the particle release but also its duration. The latter is always less than $0.5s$, to be compared with $2s$ to $4s$ for similar compression achieved from the front side. Said differently, the incomplete character of the relaxation could, at first glance, be explained by a premature arrest of the process. Yet, a more detailed analysis of our data may indicate a more complex phenomenon.

Let us start considering the front-compressed rafts, see Fig. 10(b). To interpret the release dynamics, it may be useful to make an analogy with an electric system. In this frame, the instantaneous rate of release, or flow, $-\varphi_e \dot{A}_e$, corresponds to the current i . The flow is subjected to some resistance, R , which we assume to be constant. The confined area can be modeled as a capacitor of capacitance C , whose charge q corresponds, at first order, to the excess of particles. Thus, for any instant t , $q = \varphi_j(A_r - A_c) - \varphi_e A_e$, where $\varphi_j(A_r - A_c)$ represents the initial excess of particles and $\varphi_e A_e$ the escaped particles. Noting U the potential difference, the capacitor discharge through a resistor R is given by

$$C \frac{dU}{dt} + \frac{U}{R} = 0. \quad (1)$$

This equation can be solved for given initial conditions providing $U(t)$, and by extension $i(t) = U(t)/R$. In the present system, the first term of Eq. (1), $CdU/dt = dq/dt = i$, corresponds to $-\varphi_e \dot{A}_e$ and the second one, $U/R = q/RC$, to $[\varphi_j(A_r - A_c) - \varphi_e A_e]/RC$. The discharge equation therefore becomes

$$\dot{A}_e + \frac{A_e - (A_r - A_c)\varphi_j/\varphi_e}{RC} = 0 \quad (2)$$

and the solution verifying the initial condition $A_e(t=0) = 0$ is then

$$A_e = A_0(1 - e^{-t/\tau}), \quad (3)$$

with $A_0 = (A_r - A_c)\varphi_j/\tau\varphi_e$, the final escaped surface area and $\tau = RC$, the release time constant.

The relevance of our analogy is tested by fitting the experimental evolution of A_e with Eq. (3), letting A_0 and τ be adjusted to minimize the sum of square residuals. The agreement is excellent, see Fig. 10(b). The largest deviations are indeed observed either at the very beginning or at the end. The former is attributed to initial perturbations, caused, for example, by the emission of a capillary wave, by a possible short transient regime, or by the difficulty to precisely identify the time origin. The discrepancy found in the last instants may origin a premature arrest of the relaxation, which is discussed later. The values of τ and A_0/τ produced by the fitting procedure are plotted in the inset as stars and squares, respectively. Both quantities increase roughly linearly with K . Given the limited number of points, the interpretation remains tentative but one could postulate that R , the resistance to the flow, is similar for all front-compressed rafts, while C , the system capacitance, is directly proportional to the amount of particles stored in the folds, and thus to K . The initial discharge rate given by A_0/τ also increases with K , but the linear character is less pronounced and more difficult to interpret.

Let us now focus on back-compressed rafts. The data of Fig. 10(a) cannot be immediately identified with exponential decay, which questions the previous interpretation. The latter considers the emptying of a reservoir subjected to a pressure, which decreases linearly with A_e , and to losses, which are proportional to the flow, i.e., scaling as \dot{A}_e . Given the very limited decrease of Π measured during the relaxation, it is legitimate to consider a constant pressure. Keeping the rest unchanged leads to a simple linear increase of A_e with t , which reads

$$A_e = \frac{\Pi_0}{\varphi_e R} t. \quad (4)$$

Here, Π_0 is the constant pressure applied at the back of the raft, φ_e and R are unchanged and represent the escaped particle density and the resistance to the flow, respectively. This model is confronted to the experimental results, which are fitted by linear functions, see dashed lines in Fig. 10(a). Note that not-zero intercepts are enabled since the experimental curves show an initial step. Beside this, the agreement is reasonable with the largest deviations observed at the end of the process. Interestingly, assuming that $\Pi_0 \propto A_r - A_c$, we expect the slope $\Pi_0/(\varphi_e R)$ of equal-sized rafts (constant A_r) to be proportional to K . This is indeed in good agreement with our data, see inset of Fig. 10(a), which shows—despite the limited

number of points—a linear variation of the fitted slopes with K . These curves can therefore be seen as classical emptying of granular silos. Indeed, the well-known Beverloo law predicts for given particle and orifice sizes, a constant flow rate [50]. The origin of this law remains controversial and neither the Janssen effect [51] nor the free-falling arch approach seems to provide the correct view [52]. Furthermore, the dependency of the flow rate (\dot{A}_e) with the pressure remains unclear. Some experiments evidence a total independence [48], while others show a proportional relation [53], corresponding to our findings. Independently from this controversy, it is remarkable that a transition from a viscous (clepsydralike) to a granular (sand-hour-like) emptying can apparently be triggered by the change of compression direction. Such a transition was already obtained numerically [54] and attributed to particle-particle friction. At this stage, it is worth noting that these results, i.e., a potential transition toward granular emptying with $A_e(t) \propto t$ and $\dot{A}_e \propto K$, are also compatible with the premature arrest of exponential release, and thus with a viscous regime, as found for front-compressed rafts. One must here keep in mind that the limited character of the current data does allow one to select one of the two models. Yet, whatever the chosen function, the question of why and when the relaxation process get arrested remains open.

Let us first consider the opposite locations of the folds, which systematically form on the compression side. Treating the folds as reservoirs of partly elastic energy, possible conversion into other types of energy is expected to strongly depend on the environment. For front compression, folds are at the orifice and can almost freely unfold by releasing unjammed particles out of the confined area. In contrast, folds at the back cannot unfold unless setting in motion the large raft domain sandwiched between the folds and orifice. This may naïvely be modeled by an increased resistance R . Yet this approach can only explain the kinetics slowdown (increased of $\tau = RC$), not the relaxation arrest. Thus it seems more appropriate to consider the sandwiched domain as a mechanical barrier. From a rheological point of view, this concept is closely related to the existence of a yield stress. As long as pressure Π is above a certain critical value, the raft flows. Yet, small decrease of Π , even limited and, at first order, negligible (hypothesis of constant Π_0), can stop the flow. Coming back to the electrical analogy, everything happens as if compressed rafts were granular diodes. When the diode is mounted in the appropriate direction, here corresponding to the front compression, the capacitor constituted by the particles stored in the folds can (quasi)totally discharge, the current passing through a constant resistor R . Yet, if the compression occurs from the back, the diode, mounted in the opposite direction, stops the capacitor discharge after some leaking current has passed.

C. Origin of the diode effect

This section is dedicated to the possible origins of the so-called diode effect.

It may first be understood in the light of granular framework, which describes the development of force chain networks during the compression. By moving one barrier while keeping the other fixed, chains build up, starting from

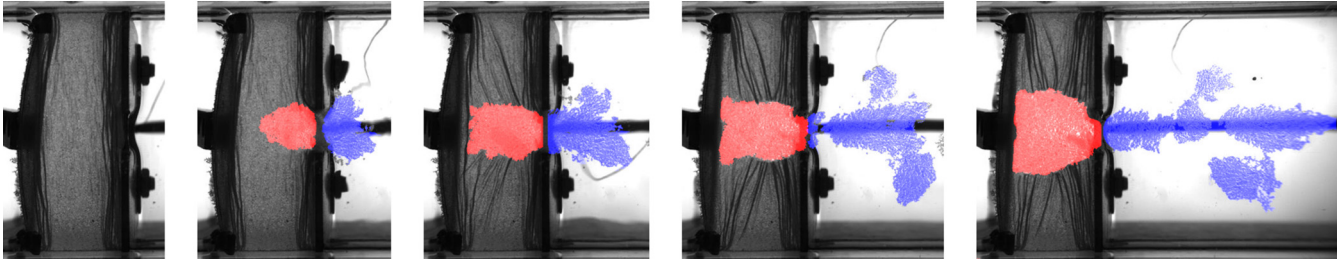


FIG. 11. Image sequences of a raft compressed from both sides ($K = 67\%$) after local release of the stress achieved by lifting the front barrier gate. From left to right: $t_1 = 0$ ms, $t_2 = 80$ ms, $t_3 = 170$ ms, $t_4 = 690$ ms, and $t_5 = 4.0$ s.

the moving barrier, and propagate via particle-particle contacts. For some of these contacts, chains divide, forming two or more branches [37]. Considering the monodisperse character of the particles, and by extension their hexagonal close packing, the orientation of these chains and branches are expected to be found in a cone, whose axis is the compression axis and angle is 60° . Consequently, for rafts compressed from the front, the keystone, i.e., particles for which the chains branch, are located right behind the gate and can therefore be easily removed after its opening, causing the force chain network to collapse, and triggering a quasitotal unjamming of the confined area. A careful inspection of the unjammed zone developing in the first instants (see Fig. 2, $t_{f,2}$) shows a conical shape, whose angle is very close to 60° , in agreement with the expected structure. In contrast, for rafts compressed from the back, an important portion of the stress building at the back is redirected on each side of the orifice. The keystones are in the back and might form arches that oppose relaxation and limit unjamming to a narrow corridor, whose width is the orifice width. Following this approach, the arch dimension is expected to exceed the orifice width, which corresponds to at least 100 particles per arch, i.e., more than one order of magnitude above values reported for dry granular [55–57]. This discrepancy may originate the capillary lateral attraction between the particles. It may also indicate that the relaxation arrest originates a different phenomenon taking place at a different scale.

To refine our interpretation, additional experiments are performed. They consist of compressing the rafts to the same levels of 33%, 50%, and 67% by simultaneously moving the back and front barriers. As before, the barriers are stopped before the gate opens. The relaxation follows an intermediate behavior, as illustrated by the images in Fig. 11 or the corresponding movie in Ref. [58]. The unjamming starts principally behind the gate; it extends laterally beyond the gate width and stops without becoming total. Remarkably, the final state is characterized by the coexistence of folds with opposite orientation. Indeed, for back-compressed rafts, the folds get advected in their center and form a **V**, which points toward the orifice; see upper sequence in Fig. 2 or left pictures in Fig. 9. In contrast, front compressed rafts show **V**-shaped structure pointing to the back; see, for example, lower sequence in Fig. 2 or remaining folded domains in Fig. 9. In the case of rafts compressed from both sides, the two orientations coexist, see Fig. 11 and Ref. [58].

This particularity is confirmed by the pictures of the raft final state obtained for other compression levels, see Fig. 12.

For completeness, this figure also shows the temporal evolution of A_e (top right) and the final values of A_{uj} (bottom right). The dynamics of the escaped assembly area is neither linear, nor exponential but rather follows two regimes. First, until approx. 0.5s, the particle flux, \dot{A}_e , is comparable to the ones observed for front or back compression, see blue continuous and dashed lines, respectively. Then, a rather linear and slow regime establishes. By carefully observing the process, this second phase can be identified with the lateral growth of the unjammed area. This slow erosion of the folded blocks eventually stops and likewise the raft relaxation. The final escaped areas A_e are found between 0.14 and 0.25, well below the values given by front compression and slightly above those provided by back compression. Interestingly, the three curves are almost identical, suggesting that the relaxation process is similarly regulated for all compression levels. Finally and despite the limited number of points, the final values of A_{uj}

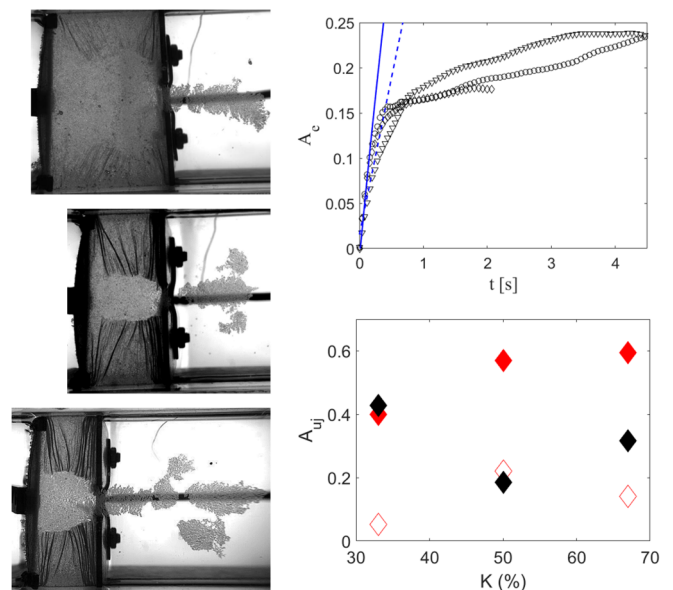


FIG. 12. Results obtained with the rafts compressed on both sides. Left: Final states with from top to bottom: $K = 33\%$, 50% , and 67% . Top right: $A_e(t)$ (black symbols) for $K = 33\%$ (triangles), 50% (diamonds) and 67% (circles). The blue continuous and dashed lines represent $\dot{A}_e(t = 0)$ for front and back compression with $K = 67\%$, respectively. Bottom right: A_{uj} (black diamonds) compared with the data obtained for front/back compression (empty/full red diamonds).

(black) are found between the ones of back (empty red symbols) and front (full red ones) compression.

These elements confirm the crucial role played by the compression direction and provide hints to better assess the scale at which the diode effect takes place. The coexistence of folds of opposite orientation, roughly extending in the front and back halves of the raft, suggests considering the fold scale. Each fold can be seen as a compressed spring, which relaxes by unfolding, thereby, only if particles can move perpendicularly to it, either in front, or behind it. Because of the back barrier, folds of back compressed rafts can only unfold toward the front. To do so, the particles sandwiched between the folds and orifice must be displaced. The combined effects of the stress directionality and the poor raft cohesion under shear leads to the extrusion of a raft portion whose width is more or less the orifice width. As a result, (some of) the folds relax but only on a central section width w . Simultaneously, the remaining folds dragged by the central flow reorientate to form a \mathbf{V} structure that points toward the orifice. This geometry, visible on the left pictures of Fig. 10, locks any further unfolding and the relaxation stops. In contrast, for front-compressed rafts, the folds can directly relax into the free interface. Thanks to the local orientation of the force chain network, the unjamming domain can expand left and right from the orifice, forming an angle of approximately 60° . This shape enables the remaining folds to gradually turn, forming a \mathbf{V} pointing toward the back, see Fig. 2 at $t_{f,2}$ and $t_{f,3}$. This geometry eventually leads the two folded blocks to unlock and the raft to totally relax. This interpretation is in agreement with the observations made with mixed compression. There, the reorientation of the front folds gets blocked by the presence of the back folds, which in turn hinders further unfolding. At this point, the flux of escaping particles considerably slows down, marking the end of the first phase. Thereafter, only a limited flux remains, which stems from the slow erosion of the folded block. Finally, this also stops. This interpretation, which combines effects at the level of the force chain network and at the one of a fold, is in agreement with all experimental results. Thus, despite its qualitative character, it constitutes a good basis for further developments. The latter may especially benefit from future investigations probing, for example, the effects of capillary lateral attraction, solid friction, or simply the influence of the orifice size and particle diameter ratio.

V. CONCLUSIONS

The relaxation behavior of strongly compressed rafts substantially depends on the compression direction of these systems. For back compressed rafts, the relaxation is incomplete whereas it is quasitotal for front compressed rafts. Practically, these results demonstrate that the processability of these interfaces is dramatically influenced by their history. In the present configuration, the flowability is primarily set by the compression direction, the level of compression playing a secondary role. This important finding should be accounted for in industrial processes. It is also of importance while considering the self-healing properties of these interfaces. The capacity of particles stored into large folds to migrate and stabilize uncovered areas is almost total for favorable compression direction, while it is drastically hindered in the

opposite case. The dynamics of the particle release itself is strongly affected by the compression direction. While the presented data remain limited, similar trends are observed in ongoing tests made with other particles or geometries.

A phenomenological model, based on the analogy with an electrical circuit, can be used. The folds act as a capacitor, the particle flux constitutes the electrical current, the mechanical losses are accounted for via a resistor, and the effects of the compression direction are reproduced by a diode. Physically, the diode effect could be attributed to a locking mechanism. It may originate the orientation of the force chain network, a structure which is expected to form in the rafts as in any granular matter. It may also develop at the fold level, each fold playing the role of a compressed spring, whose possible relaxation is subjected to local constrains.

Finally, it is worth noting that our results and interpretation give rise to many open questions which need to be treated in future research. From our point of view, future investigations should aim in understanding the relative importance of the force chain network and the raft folds. In this frame, we can of course think of varying the raft and trough geometry, and especially the raft length, its width, and the size of the orifice. A second important aspect is the influence of the individual particles and, more particularly, the role of friction, shape, but also possible contact lubrication, which could, for example, cause aging and reduce raft cohesion.

ACKNOWLEDGMENTS

We would like to thank the Austrian Science Fund (FWF) for financial support under Grant No. P33514-N. We also acknowledge Graz University of Technology for its technical support, especially the Institute of Hydraulic Engineering and Water Resources Management for lending us the high-speed camera and the Institute of Process and Particle Engineering for helping us sieve the particles. C.P. acknowledges Elise Lorenceau and Anne-Laure Bianco for fruitful discussions.

APPENDIX A: ELASTIC RUBBER PREPARATION

The elastic rubber strings are produced in-house by injecting a freshly prepared (1:1) mixture of Zhermack Elite Double 8 basis and catalyst (Zhermac Spa) into glass capillaries. After the elastomer reticulation has been completed, the glass capillaries are manually removed. Using capillaries of various diameter, we produce strings whose diameter ranges between 0.5 and 1 mm. Their typical length is in the range of 10 cm, which is sufficient to be installed in a 6-cm-wide trough.

APPENDIX B: RUBBER CALIBRATION

The calibration of the rubber mostly consists of determining its Young's modulus. The principle, detailed below, is simple, and consists of measuring the deflections produced by hanging known weights to the rubber, see Fig. 13. It was presented in the Ph.D. thesis of Pauline Petit [59].

Consider an elastic string of relaxed length s_0 (not precisely known), attached between two holders separated by s_1 (black rectangles in Fig. 13). The elastic is further loaded using a known mass m ($F_g = mg$) and reaches a stretched length

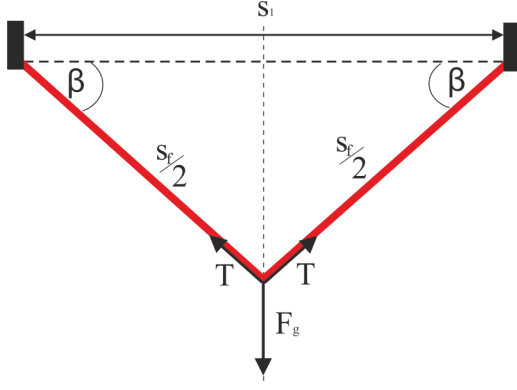


FIG. 13. Principle of the elastic calibration: Deformation is measured as a function of the applied force.

s_f , which can easily be measured. The tensile stress, σ , is linearly proportional to the strain, ϵ , and the proportionality coefficient, E , is the Young's modulus. This reads

$$\sigma = E\epsilon. \quad (\text{B1})$$

The strain is equal to the relative extension and the tensile stress derives from the tension T , providing

$$\epsilon = \frac{s_f - s_0}{s_0} \quad \text{and} \quad \sigma = \frac{T}{\Sigma}, \quad (\text{B2})$$

with Σ the cross-section area of the elastic string under tension. The Hook's law may now be rewritten as

$$T = E \Sigma \frac{s_f - s_0}{s_0} = E \Sigma_0 \frac{s_f - s_0}{s_f}, \quad (\text{B3})$$

where the variation of the cross-section area due to the stretching was introduced as

$$\Sigma = \Sigma_0 \frac{s_0}{s_f}. \quad (\text{B4})$$

Σ_0 is the cross-section area of the nondeformed elastic string. Under a small load, the force equilibrium may be written as

$$F_g = 2T \sin \beta \quad \text{with} \quad \sin \beta = \sqrt{1 - \left(\frac{s_1}{s_f}\right)^2}. \quad (\text{B5})$$

Here, β is the angle between the rubber string and the horizontal. Combining the above equations, one obtains the following relationship:

$$mg = 2\lambda_0 \cdot \frac{s_f - s_0}{s_f} \sqrt{1 - \left(\frac{s_1}{s_f}\right)^2}, \quad (\text{B6})$$

with our introduced parameter λ_0 , defined by $\lambda_0 = E \Sigma_0$.

Practically, the length of the deformed rubber s_f is measured from pictures taken for different known masses m . The undeformed rubber length, s_0 , which is not precisely known, and the parameter λ_0 are then obtained by finding the best fit to the measured data. This is done with the help of the `fminsearch` function of MATLAB. An illustrative curve is displayed in Fig. 14. The coefficient of regression is always very close to one, greater than 0.99. The 95% confident intervals corresponds to an uncertainty of $\pm 1\%$ on λ_0 and s_0 . Knowing

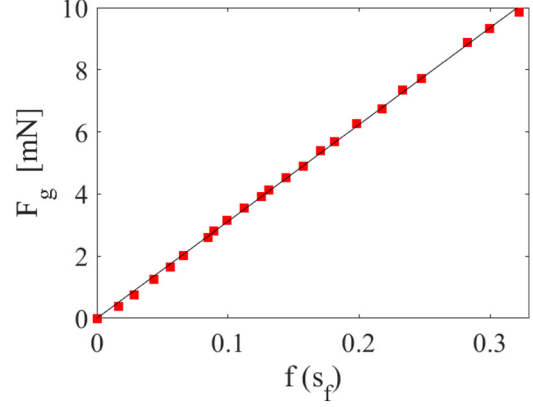


FIG. 14. Typical calibration curve and its linear fit providing s_0 (here 44.46 mm) and λ_0 (here 0.3152 N). Function f is defined as $f(s_f) = 2 \frac{s_f - s_0}{s_0} \sqrt{1 - \frac{s_1^2}{s_f^2}}$. The coefficient of regression is $R^2 = 0.9995$.

Σ_0 , the cross section of the undeformed string, the modulus of elasticity is finally deduced as

$$E = \frac{\lambda_0}{\Sigma_0}. \quad (\text{B7})$$

Using Elite Double 8, the measured E is found to be in the expected range of 0.1 MPa. Note that the two parameters s_0 and λ_0 are also necessary to describe the deformation of the elastic string subjected to a constant lineic force, as shown in the next Appendix.

APPENDIX C: DEFORMATION EQUATIONS

The calibrated rubber string can then be used as a pressure sensor for the particle rafts in our experiments. To be quantitative, the relationship between the elastic deflection, δ , and the applied lineic pressure, Π , is needed. These quantities are defined in Fig. 15. The length of the stretched elastic is s_f , as previously defined. The position along the elastic can be described by the curvilinear ordinate s or by the cartesian coordinates (x, y) , the x - and y -axes have unit vectors \hat{x} and \hat{y} , respectively. The following derivation is based on the well-known mathematical problem of a classical catenary [60]. The tension \vec{T} has a norm (T) and is collinear to the string at any point $s \in [-s_f/2; s_f/2]$. Thus, naming T_x and T_y its horizontal

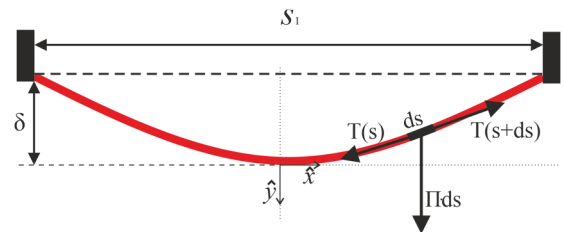


FIG. 15. Deformation of an elastic string due to the action of constant lineic force Π .

and vertical components, we get

$$\frac{dy}{dx} = \frac{T_y}{T_x} \quad \text{and} \quad T = \sqrt{T_x^2 + T_y^2}. \quad (\text{C1})$$

Using the definition of the lineic pressure, Π , and applying the force balance to a string element of infinitesimal length ds (see Fig. 15) provides

$$T_y = \int_0^{s_f/2} \Pi ds = \Pi \int_0^{s_f/2} ds, \quad (\text{C2})$$

which leads with Eq. (C1) to

$$\frac{dy}{dx} = \frac{\Pi}{T_x} \int_0^{s_f/2} ds, \quad ds = \frac{\Pi}{T_x} \int_0^{s_1/2} \frac{ds}{dx} dx. \quad (\text{C3})$$

Equation (C3) can be differentiated with respect to x , leading to

$$\frac{d^2y}{dx^2} = \frac{\Pi}{T_x} \frac{ds}{dx}. \quad (\text{C4})$$

To go further, the curvilinear ordinate is eliminated using

$$ds^2 = dx^2 + dy^2 = dx^2 \left(1 + \left(\frac{dy}{dx} \right)^2 \right), \quad (\text{C5})$$

which also writes

$$\frac{ds}{dx} = \sqrt{1 + \left(\frac{dy}{dx} \right)^2}. \quad (\text{C6})$$

Equation (C4) becomes

$$\frac{d^2y}{dx^2} = \frac{\Pi}{T_x} \sqrt{1 + \left(\frac{dy}{dx} \right)^2}. \quad (\text{C7})$$

It is integrated with boundary conditions $dy/dx(x=0) = 0$ and $y(x=0) = 0$, providing

$$y(x) = \frac{T_x}{\Pi} \left(\cosh \left(\frac{\Pi}{T_x} x \right) - 1 \right). \quad (\text{C8})$$

Evaluating this expression for $x = s_1/2$ gives the central string deflection:

$$\delta = \frac{T_x}{\Pi} \left(\cosh \left(\frac{\Pi s_1}{2T_x} \right) - 1 \right). \quad (\text{C9})$$

In practice, to use this expression, it is necessary to explicit T_x as a function of the known parameters, i.e., s_1 , s_0 , and λ_0 . Combining Eqs. (C1) and (C2), we get

$$T = \sqrt{T_x^2 + \left(\Pi \int_0^{s_f/2} ds \right)^2}. \quad (\text{C10})$$

Using the stress-strain relation from the calibration section [Eq. (B3)] and the definition of the parameter λ_0 given by Eq. (B7), we identify T , with

$$T = \lambda_0 \frac{s_f - s_0}{s_f}, \quad (\text{C11})$$

and obtain

$$\lambda_0 \frac{s_f - s_0}{s_f} = \sqrt{T_x^2 + \left(\Pi \int_0^{s_f/2} ds \right)^2}. \quad (\text{C12})$$

We then eliminate s_f using

$$\begin{aligned} \frac{s_f}{2} &= \int_0^{s_f/2} ds = \int_0^{s_1/2} \sqrt{1 + \left(\frac{dy}{dx} \right)^2} dx \\ &= \frac{T_x}{\Pi} \sinh \left(\frac{\Pi s_1}{2T_x} \right). \end{aligned} \quad (\text{C13})$$

Equations (C12) and (C13) provide the condition

$$\lambda_0 \frac{\frac{T_x}{\Pi} \sinh \left(\frac{\Pi s_1}{2T_x} \right) - \frac{s_0}{2}}{\frac{T_x}{\Pi} \sinh \left(\frac{\Pi s_1}{2T_x} \right)} = \sqrt{T_x^2 \left(1 + \sinh^2 \left(\frac{\Pi s_1}{2T_x} \right) \right)} \quad (\text{C14})$$

or, equivalently,

$$T_x \cosh \left(\frac{\Pi s_1}{2T_x} \right) = \lambda_0 \left(1 - \frac{s_0 \Pi}{2T_x \sinh \left(\frac{\Pi s_1}{2T_x} \right)} \right). \quad (\text{C15})$$

The relation between δ , the central deflection of the elastic string, and Π , the applied lineic pressure is therefore given by the two equations (C9) and (C15). Note that using Eq. (C8) and (C15), the entire shape of the elastic is indeed described as a function of known and measurable parameters, namely, s_1 , s_0 , and λ_0 .

For small deformations, Eqs. (C9) and (C15) can be simplified by a third-order series expansion with the approximation

$$\frac{dy}{dx} \approx \frac{s_1 \Pi}{T_x}, \quad (\text{C16})$$

which provides the following relation between the lineic pressure Π and the (small) central deflection δ :

$$\Pi = \frac{8\lambda_0}{s_1} \left[\left(1 - \frac{s_0}{s_1} \right) \frac{\delta}{s_1} + \left(\frac{4s_0}{3s_1} - 1 \right) \left(\frac{2\delta}{s_1} \right)^3 \right]. \quad (\text{C17})$$

When applying the lineic pressure measurement method described above, a non-negligible uncertainty must be taken into account. The accuracy depends strongly on the difference $s_1 - s_0$ as shown below:

$$\frac{\Delta \Pi}{\Pi} = 2 \frac{\Delta s_1}{s_1} + \frac{s_1 \Delta s_0 + s_0 \Delta s_1}{s_1 (s_1 - s_0)}. \quad (\text{C18})$$

In the present article, we evaluate this uncertainty to approximately 15%.

[1] W. Ramsden, Separation of solids in the surface-layers of solutions and 'suspensions' (observations on surface-membranes, bubbles, emulsions, and mechanical coagulation). Preliminary account, *Proc. R. Soc. London* **72**, 156 (1903).

[2] S. U. Pickering, Emulsions, *J. Chem. Soc.* **91**, 2001 (1907).

[3] O. Pitois and F. Rouyer, Rheology of particulate rafts, films, and foams, *Curr. Opin. Colloid Interface Sci.* **43**, 125 (2019).

- [4] B. P. Binks, Particles as surfactants—similarities and differences, *Curr. Opin. Colloid Interface Sci.* **7**, 21 (2002).
- [5] E. M. Herzig, K. A. White, A. B. Schofield, W. C. K. Poon, and P. S. Clegg, Bicontinuous emulsions stabilized solely by colloidal particles, *Nat. Mater.* **6**, 966 (2007).
- [6] M. E. Cates and P. S. Clegg, Bijels: A new class of soft materials, *Soft Matter* **4**, 2132 (2008).
- [7] P. Aussillous and D. Quéré, Liquid marbles, *Nature (London)* **411**, 924 (2001).
- [8] M. Abkarian, S. Protière, J. M. Aristoff, and H. A. Stone, Gravity-induced encapsulation of liquids by destabilization of granular rafts, *Nat. Commun.* **4**, 1 (2013).
- [9] E. Jambon-Puillet, C. Josserand, and S. Protière, Drops floating on granular rafts: A tool for liquid transport and delivery, *Langmuir* **34**, 4437 (2018).
- [10] N. Pike, D. Richard, W. Foster, and L. Mahadevan, How aphids lose their marbles, *Proc. R. Soc. Lond. B* **269**, 1211 (2002).
- [11] P. A. Kralchevsky, N. D. Denkov, and K. D. Danov, Particles with an undulated contact line at a fluid interface: Interaction between capillary quadrupoles and rheology of particulate monolayers, *Langmuir* **17**, 7694 (2001).
- [12] V. Garbin, Collapse mechanisms and extreme deformation of particle-laden interfaces, *Curr. Opin. Colloid Interface Sci.* **39**, 202 (2019), Special Topic Section: Outstanding Young Researchers in Colloid and Interface Science.
- [13] S. Reynaert, P. Moldenaers, and J. Vermant, Interfacial rheology of stable and weakly aggregated two-dimensional suspensions, *Phys. Chem. Chem. Phys.* **9**, 6463 (2007).
- [14] P. Cicuta, E. J. Stancik, and G. G. Fuller, Shearing or Compressing a Soft Glass in 2D: Time-Concentration Superposition, *Phys. Rev. Lett.* **90**, 236101 (2003).
- [15] G. Lagubeau, Interfaces à grains, et autres situations de mouillage nul, Ph.D. thesis, Université de Paris, 2010.
- [16] R. Aveyard, J. H. Clint, D. Nees, and N. Quirke, Structure and collapse of particle monolayers under lateral pressure at the octane/aqueous surfactant solution interface, *Langmuir* **16**, 8820 (2000).
- [17] C. Monteux, J. Kirkwood, H. Xu, E. Jung, and G. G. Fuller, Determining the mechanical response of particle-laden fluid interfaces using surface pressure isotherms and bulk pressure measurements of droplets, *Phys. Chem. Chem. Phys.* **9**, 6344 (2007).
- [18] A. J. Liu and S. R. Nagel, Jamming is not just cool any more, *Nature (London)* **396**, 21 (1998).
- [19] P. Sollich, F. Lequeux, P. Hébraud, and M. E. Cates, Rheology of Soft Glassy Materials, *Phys. Rev. Lett.* **78**, 2020 (1997).
- [20] P. Hébraud and F. Lequeux, Mode-Coupling Theory for the Pasty Rheology of Soft Glassy Materials, *Phys. Rev. Lett.* **81**, 2934 (1998).
- [21] P. J. Beltramo, M. Gupta, A. Aliche, I. Liascukiene, D. Z. Gunes, C. N. Baroud, and J. Vermant, Arresting dissolution by interfacial rheology design, *Proc. Natl. Acad. Sci.* **114**, 10373 (2017).
- [22] N. Taccoen, F. Lequeux, D. Z. Gunes, and C. N. Baroud, Probing the Mechanical Strength of an Armored Bubble and its Implication to Particle-Stabilized Foams, *Phys. Rev. X* **6**, 011010 (2016).
- [23] M. Abkarian, A. B. Subramaniam, S. H. Kim, R. J. Larsen, S. M. Yang, and H. A. Stone, Dissolution Arrest and Stability of Particle-Covered Bubbles, *Phys. Rev. Lett.* **99**, 188301 (2007).
- [24] Y. Timounay and F. Rouyer, Viscosity of particulate soap films: Approaching the jamming of 2D capillary suspensions, *Soft Matter* **13**, 3449 (2017).
- [25] S. T. Milner, J. Joanny, and P. Pincus, Buckling of Langmuir monolayers, *Europhys. Lett.* **9**, 495 (1989).
- [26] W. Helfrich, Elastic properties of lipid bilayers: Theory and possible experiments, *Z. Naturforsch. C* **28**, 693 (1973).
- [27] E. Cerda and L. Mahadevan, Geometry and Physics of Wrinkling, *Phys. Rev. Lett.* **90**, 074302 (2003).
- [28] L. Pocivavsek, R. Dellsy, A. Kern, S. Johnson, B. H. Lin, K. Y. C. Lee, and E. Cerda, Stress and fold localization in thin elastic membranes, *Science* **320**, 912 (2008).
- [29] D. Vella, P. Aussillous, and L. Mahadevan, Elasticity of an interfacial particle raft, *Europhys. Lett.* **68**, 212 (2004).
- [30] C. Planchette, E. Lorenceau, and A. L. Biance, Surface wave on a particle raft, *Soft Matter* **8**, 2444 (2012).
- [31] P. Petit, A.-L. Biance, E. Lorenceau, and C. Planchette, Bending modulus of bidisperse particle rafts: Local and collective contributions, *Phys. Rev. E* **93**, 042802 (2016).
- [32] P. Cicuta and D. Vella, Granular Character of Particle Rafts, *Phys. Rev. Lett.* **102**, 138302 (2009).
- [33] O. Pitois, M. Buisson, and X. Chateau, On the collapse pressure of armored bubbles and drops, *Eur. Phys. J. E* **38**, 48 (2015).
- [34] D. Vella, H. Y. Kim, P. Aussillous, and L. Mahadevan, Dynamics of Surfactant-Driven Fracture of Particle Rafts, *Phys. Rev. Lett.* **96**, 178301 (2006).
- [35] M. Basavaraj, G. Fuller, J. Fransaer, and J. Vermant, Packing, flipping, and buckling transitions in compressed monolayers of ellipsoidal latex particles, *Langmuir* **22**, 6605 (2006).
- [36] O. Saavedra V., H. Elettro, and F. Melo, Progressive friction mobilization and enhanced Janssen's screening in confined granular rafts, *Phys. Rev. Mater.* **2**, 043603 (2018).
- [37] T. S. Majmudar and R. P. Behringer, Contact force measurements and stress-induced anisotropy in granular materials, *Nature (London)* **435**, 1079 (2005).
- [38] J. F. Peters, M. Muthuswamy, J. Wibowo, and A. Tordesillas, Characterization of force chains in granular material, *Phys. Rev. E* **72**, 041307 (2005).
- [39] A. Tordesillas, Q. Lin, J. Zhang, R. Behringer, and J. Shi, Structural stability and jamming of self-organized cluster conformations in dense granular materials, *J. Mech. Phys. Solids* **59**, 265 (2011).
- [40] D. Fischer, R. Stannarius, K. Tell, P. Yu, and M. Sperl, Force chains in crystalline and frustrated packing visualized by stress-birefringent spheres, *Soft Matter* **17**, 4317 (2021).
- [41] C. Planchette, E. Lorenceau, and A.-L. Biance, Rupture of granular rafts: Effects of particle mobility and polydispersity, *Soft Matter* **14**, 6419 (2018).
- [42] V. Garbin, Colloidal particles: Surfactants with a difference, *Phys. Today* **66**(10), 68 (2013).
- [43] I. Arganda-Carreras, V. Kaynig, C. Rueden, K. W. Eliceiri, J. Schindelin, A. Cardona, and H. Sebastian Seung, Trainable Weka Segmentation: A machine learning tool for microscopy pixel classification, *Bioinformatics* **33**, 2424 (2017).
- [44] W. Thielicke and E. Stamhuis, PIVlab—Towards user-friendly, affordable and accurate digital particle image velocimetry in MATLAB, *J. Open Res. Software* **2**, e30 (2014).

- [45] W. Thielicke and R. Sonntag, Particle image velocimetry for MATLAB: Accuracy and enhanced algorithms in PIVlab, *J. Open Res. Software* **9**, 12 (2021).
- [46] See Supplemental Material at <http://link.aps.org/supplemental/10.1103/PhysRevE.106.034903> for the movie showing the relaxation of the *back* compressed raft (67% compression).
- [47] See Supplemental Material at <http://link.aps.org/supplemental/10.1103/PhysRevE.106.034903> for the movie showing the relaxation of the *front* compressed raft (67% compression).
- [48] M. A. Aguirre, J. G. Grande, A. Calvo, L. A. Pagnaloni, and J.-C. Géminard, Pressure Independence of Granular Flow Through an Aperture, *Phys. Rev. Lett.* **104**, 238002 (2010).
- [49] M. A. Aguirre, J. G. Grande, A. Calvo, L. A. Pagnaloni, and J.-C. Géminard, Granular flow through an aperture: Pressure and flow rate are independent, *Phys. Rev. E* **83**, 061305 (2011).
- [50] W. A. Beverloo, H. A. Leniger, and J. Van de Velde, The flow of granular solids through orifices, *Chem. Eng. Sci.* **15**, 260 (1961).
- [51] H. Janssen, Versuche uber getreidedruck in silozellen, *Z. Ver. Dtsch. Ing.* **39**, 1045 (1895).
- [52] S. M. Rubio-Largo, A. Janda, D. Maza, I. Zuriguel, and R. C. Hidalgo, Disentangling the Free-Fall Arch Paradox in Silo Discharge, *Phys. Rev. Lett.* **114**, 238002 (2015).
- [53] Z. Peng, J. Zhou, J. Zhou, Y. Miao, L. Cheng, Y. Jiang, and M. Hou, External pressure dependence of granular orifice flow: Transition to Beverloo flow, *Phys. Fluids* **33**, 043313 (2021).
- [54] L. Staron, P.-Y. Lagrée, and S. Popinet, The granular silo as a continuum plastic flow: The hour-glass vs the clepsydra, *Phys. Fluids* **24**, 103301 (2012).
- [55] I. Zuriguel, A. Janda, A. Garcimartín, C. Lozano, R. Arévalo, and D. Maza, Silo Clogging Reduction by the Presence of an Obstacle, *Phys. Rev. Lett.* **107**, 278001 (2011).
- [56] A. Nicolas, A. Garcimartín, and I. Zuriguel, Trap Model for Clogging and Unclogging in Granular Hopper Flows, *Phys. Rev. Lett.* **120**, 198002 (2018).
- [57] B. V. Guerrero, B. Chakraborty, I. Zuriguel, and A. Garcimartín, Nonergodicity in silo unclogging: Broken and unbroken arches, *Phys. Rev. E* **100**, 032901 (2019).
- [58] See Supplemental Material at <http://link.aps.org/supplemental/10.1103/PhysRevE.106.034903> for the movie showing the relaxation of the raft compressed simultaneously on *both sides* ($k = 67%$).
- [59] P. Petit, Déformation des interfaces complexes: Des architectures savonneuses aux mousses de particules, Ph.D. thesis, University of Lyon, 2014.
- [60] A. Borggräfe, J. Heiligers, M. Ceriotti, and C. R. McInnes, Shape control of slack space reflectors using modulated solar pressure, *Proc. R. Soc. A* **471**, 20150119 (2015).